Ocean Dynamics (2018) 68:1221–1237
https://doi.org/10.1007/s10236-018-1197-x

Experimental investigation on sea ripple evolution over sloping beaches

Carmelo Petrotta[1] · **Carla Faraci**[1] · **Pietro Scandura**[2] · **Enrico Foti**[2]

Received: 15 October 2017 / Accepted: 3 July 2018 / Published online: 14 July 2018

Abstract

This paper reports on a wave flume experimental campaign carried out to investigate the appearance, the growth and the migration of small scale bedforms on a sloping sandy bed due to both regular and random waves. A Vectrino Profiler along with a structured light approach were used for velocity and morphodynamic measurements at two positions, one located above the horizontal bed, and the other one above the sloping beach. The velocity was computed by phase averaging the velocity measurements. Several velocity profiles were analyzed, identifying an offshore-directed steady current that extends from few centimeters above the bottom for all the analyzed water column. Ripple geometry was measured by a structured light approach and compared with that predicted by several models to shed light on the effects induced by the sloping beach on the shape and asymmetry. Along the sloping beach, the ripples appeared strongly asymmetric with the onshore half wavelengths smaller than the offshore ones. Finally, ripple geometry and migration triggered by regular waves were compared with those generated by random waves with comparable flow orbital amplitude showing a good agreement.

Keywords Bedform morphodynamics · Hydrodynamics · Ripples · Sloping beach · Equilibrium conditions

1 Introduction

In the nearshore zone, the gravity wave propagation over a non-cohesive sandy bed can cause the appearance of small scale bedforms known as ripples. These bedforms have a significant influence on the structure of the boundary layer, on the wave energy dissipation as well as on the sediment transport mechanism. Due to their relevance for coastal hydromorphodynamics, a large number of studies have been devoted to investigate ripple formation, evolution and the assessment of an equilibrium condition, as well as their velocity of migration (e.g., Sleath 1984; Blondeaux 1990).

Ripples first appear on a flat sandy bed subject to an oscillatory flow in the form of rolling grain ripples (Bagnold 1946). Then, they quickly evolve to vortex ripples, the latter characterized by vortices detaching alternatively during each half cycle from the ripple crests. Several studies were aimed at assessing the existence of equilibrium conditions, based on the oscillatory flow characteristics. Ripple predictor models were proposed, among others, by Nielsen (1981), Van Rijn (1993), and Faraci and Foti (2002) as a function of flow parameters. By means of a linear stability analysis, Blondeaux et al. (2000) found that wave non-linearities together with the spatial non-uniformity of the boundary layer induce a steady velocity component in the direction of wave propagation. As a consequence, ripple migration occurs at a constant rate that depends on both sediment and wave characteristics. Measurements in an oscillatory water tunnel over sand ripples showed the presence of steady circulation cells with a dominant offshore mean flow (Van der Werf et al. 2007). These

Responsible Editor: Troels Aagaard

This article is part of the Topical Collection on the *8th International Conference on Coastal Dynamics, Helsingør, Denmark, 12–16 June 2017*

✉ Carmelo Petrotta
cpetrotta@unime.it

Carla Faraci
cfaraci@unime.it

Pietro Scandura
pietro.scandura@unict.it

Enrico Foti
enrico.foti@unict.it

[1] Department of Engineering, University of Messina, C.da di Dio, 98166 S. Agata, Messina, Italy

[2] Department of Civil Engineering and Architecture, University of Catania, v.le A. Doria 6, 95125 Catania, Italy

authors observed that although the measured net time-averaged suspended sand flux was offshore directed, the ripple migration was dominated by the onshore-directed bedload.

In fact, a crucial influence on the direction and the net rate of sand transport, as well as on the bedform characteristics is exerted by the flow asymmetry. In this perspective, several studies were recently focused on the effects that an asymmetrical oscillatory flow may have on an uneven bottom, both in terms of ripple characteristics and on sediment transport rate. A possible effect of the wave asymmetry is that ripples become asymmetric as soon as the mass transport velocity induced by wave asymmetry itself increases. In particular, when considering asymmetrical waves, O'Donoghue et al. (2006) observed that full-scale measurements of ripples are well described by Nielsen (1981) model. Doucette and O'Donoghue (2006) investigated the ripple evolution from a flat to a rippled bed under different flow conditions. They showed that both the time to reach equilibrium and the equilibrium ripple shape strongly depend on the flow field, whereas ripples are independent on the initial bed morphology. More recently, Blondeaux et al. (2015) through a weakly non-linear stability analysis of a flat sandy bottom subjected to an oscillatory flow related the symmetry index of the ripples to wave and sediment characteristics. They found that the steady current makes the onshore flank of the ripples steeper than the offshore side.

In nature, flow asymmetry is due to non-linearities, which are enhanced when spatial variability is important. An example is the case of a sloping beach. In this case, the wave flow interaction with the bed may lead the waves to become skewed, with sharp crest and flat trough, and asymmetric, with a steep front and a gently sloping rear face. As a consequence, the onshore-directed near-bed acceleration is larger than that in the offshore direction, thus giving rise to an acceleration-skewed flow Scandura et al. (2016). Such a phenomenon affects the hydrodynamics, generating an important steady drift, which in turn, impacts on coastal sediment transport (Hsu and Hanes 2004).

Bed slope effects on the wave boundary layers were first studied analytically by Bijker et al. (1974) in the laminar case. Later on, Sumer et al. (1993) performed an experimental campaign on turbulent oscillatory boundary layers in a convergent channel. The data acquired by Sumer et al. (1993) showed that a constant streaming near the wall in the direction towards the convergent end of the channel exists and that in the convergent half period turbulence is largely dampened. Fuhrman et al. (2009a) used the RANS equations coupled with a $k-\omega$ turbulence closure, in order to simulate converging or diverging flows under rough turbulent conditions, and tested the results against the data of Sumer et al. (1993). They argued that the sloping bed influences the propagating flow likewise a convergent. Indeed, moving in the uphill direction, the pressure gradient becomes smaller and velocities higher, whereas in the downhill direction the opposite occurs. The flow near the bed during the onshore half-cycle, therefore, exceeds that of the offshore half-cycle. In an oscillatory flow, this causes the appearance of an onshore streaming that, in turn, is compensated by an offshore period averaged flow. Then, Fuhrman et al. (2009b) compared the effects of the bed slope on the flow with those caused by other factors, e.g., wave skewness, asymmetry, and steady streaming. They observed that both bed load and shear stresses are considerably influenced by a sloping beach. Even under a purely oscillatory flow, the critical Shields parameter for incipient sediment motion become different from the uphill to the downhill direction because of the gravity. This creates a net downhill (offshore) bed load that could cause an offshore ripple migration.

However, to the authors' knowledge, neither numerical simulation nor physical modeling has dealt with ripple formation and evolution over a sloping beach, where wave modifications give rise to asymmetric and skewed flow.

In this paper, the results of an experimental campaign aimed at analyzing the hydrodynamics and the morphodynamics generated by waves propagating over a sloping beach are presented. The effects of the wave asymmetry on velocity profiles, ripple shape and migration velocity were analyzed pointing out the effects induced by the sloping bed. The reliability of some models in predicting the shape of ripples triggered by both random and regular waves was also examined.

2 Experimental setup and procedure

The experiments were carried out in the wave flume of the Hydraulics Laboratory of the University of Messina (Italy). The flume is 18-m long, 0.40-m wide, and 0.80-m high with flat stainless steel bottom and glass walls (Fig. 1a).

Waves were generated within the flume by means of a flap-type wavemaker, which is able to reproduce both regular and random waves characterized by wave heights up to 0.12 m and wave periods between 0.5 and 2 s. The wavemaker was driven by a pneumatic system and was electronically controlled.

At the back of the wavemaker, some mattresses of creased pipe pieces were placed to absorb any spurious reflection caused by the flap motion. More details on the experimental setup can be found in Liu and Faraci (2014) and Faraci (2018).

Starting 8 m away from the wavemaker and for the remaining flume length, the bottom was covered with a layer 0.2-m thick of uniform sand, characterized by a median

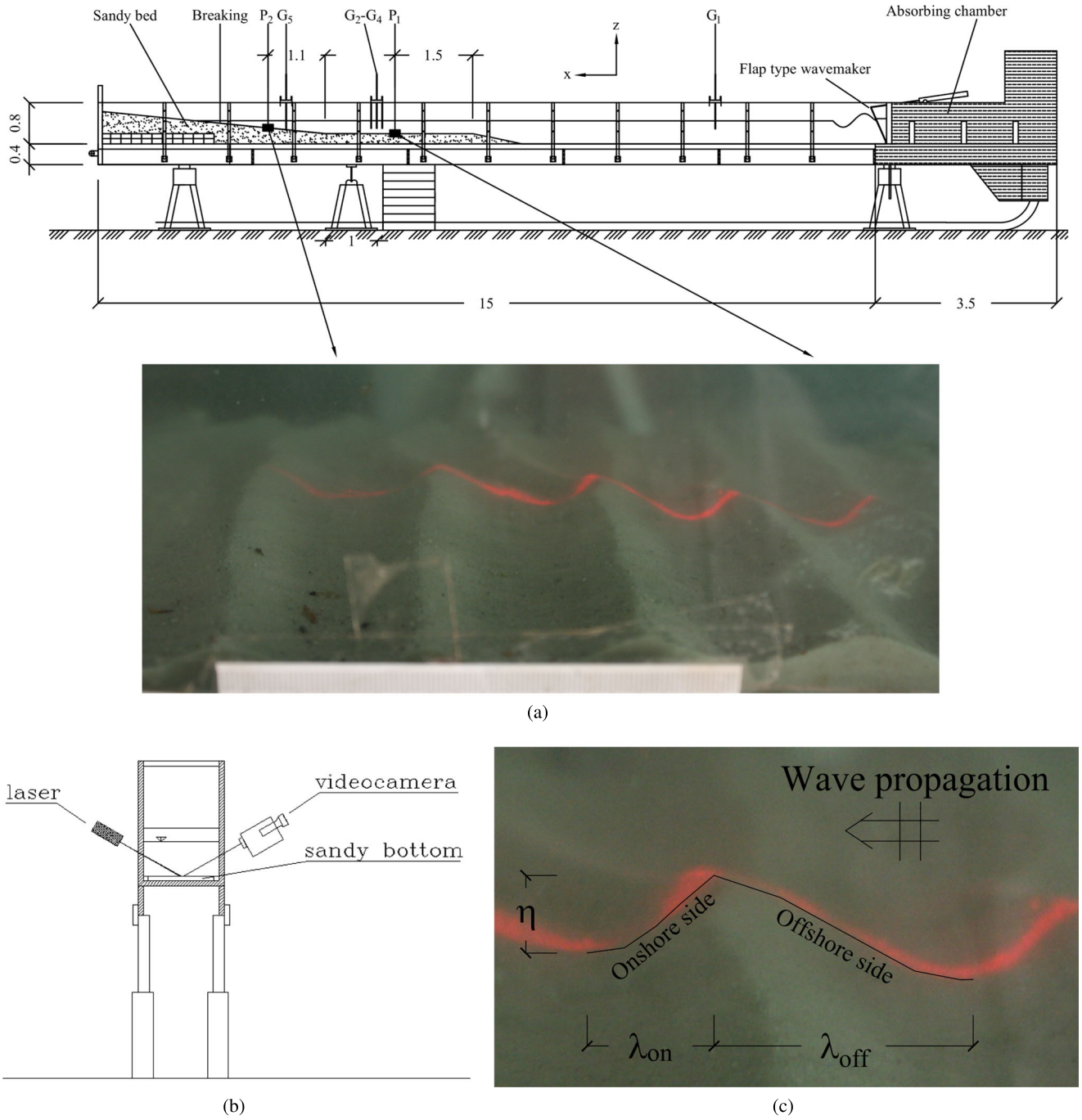

Fig. 1 Experimental setup adopted in the present experimental campaign: **a** wave flume together with a rippled bed overview; **b** sketch of the optical structured light technique; **c** laser light on the sandy bottom showing the two half wavelengths λ_{on} and λ_{off} and the height η; **d** ripple picture

grain size $d_{50} = 0.25$ mm. Farther, a plane beach, 3.5 m long with a slope of 1:10, was built oppositely to the wavemaker in order to minimize reflection. Moreover, the plane beach had the role of triggering the asymmetry of the waves propagating along the flume.

Measurements of wave characteristics throughout the wave flume were performed by means of five resistive wave gauges. The first one (G_1) was located 3.25 m off the wavemaker, three of them (G_2, G_3, G_4) were placed on the horizontal sand layer and spaced in such a way to allow the wave reflection along the flume to be evaluated by means of Mansard and Funke (1980) method. In particular, wave reflection along the flume was always comprised between 15 and 20% of the incident wave. Only for largest wave periods reflection grows up to 30%. The last gauge (G_5) was located on the sloping beach where the waves shoal.

Velocity profiles were acquired by means of a Vectrino Profiler (Nortek As.) in two positions, the first one located 1.5 m far from the beginning of the sandy bed (position P_1) and the second one located 1.1 m after the beginning of the slope (position P_2) (see Fig. 1a). The sampling volume of the probe extends from 40 mm down to 74 mm below the transducer, typically divided into 34 measuring cells with a 1-mm resolution and sampling rate equal to 100 Hz.

The reliability of the measured velocities is related to two parameters named correlation (COR) and signal to noise ratio (SNR), (see, e.g., van der Zanden et al. 2017; Yoon and Cox 2010). Two acceptance thresholds were adopted: COR $\geq$ 90 and SNR $\geq$ 30 near the sweet spot, i.e., from 50 to 65 mm below the transceiver, SNR $\geq$ 20 elsewhere. Non-reliable data were replaced by a linear interpolation. Finally, data were despiked by means of the Goring and Nikora (2002) method. To improve data integrity, the power level was set on high value, and some talc powder was dispersed near the probe head to increase the number of scatterers in the sampling volume. Moreover, in one of the performed tests (Reg_2), the velocity profiles were acquired once with a cell size parameter equal to 1 mm and a second time with a cell size of 2 mm. However, important differences were not observed comparing the two obtained profiles; hence, a cell size equal to 1 mm was adopted for the remaining tests.

Profiles were obtained by vertically overlapping each measurement station by a certain amount. This is necessary in order to be able to remove the lower part of the sampling volume data, characterized by low SNR because of sound reflection from the bottom, without producing any gap in the profiles. When vertically moving from a position to another along the profile, the sensor position is shifted up by an amount Δz each 2 min. In order to get the proper overlap between two successive stations, in most of the tests, Δz was kept equal to 2 cm, but in some tests, it was reduced to 1 or 0.5 cm, in order to reconstruct the entire velocity profile. This operation took about 10 min on the sloping bed, where the water depth was about 0.14 m, and 20 min on the horizontal plane, where the water depth was about 0.24 m. Finally, due to the near-bed acoustic interference together with the high near-bed suspended sediment concentration (see Thomas et al. 2017), data within 2 mm from the bottom were discarded (see Koca et al. 2017; Wengrove and Foster 2014).

The bed morphology was acquired by means of a structured light optical system (for details on the technique Faraci and Foti 2002; Faraci et al. 2012). A Canon EOS 450D camera with a 6.4-MP resolution and a $\pm$ 1 mm accuracy was used. The light sheet optically slices the measured body creating a cross-sectional image that can be observed and recorded through a video camera, and then analyzed to obtain the ripple dimensions (Fig. 1b and c). Once the image (Fig. 1a) was gathered by the video camera, suitable image processing procedures were adopted, in particular, the correspondence between the image units, given in pixels, and the object dimensions was determined. This task was accomplished by acquiring the image of a known object and deriving the coefficients, which give the unit dimension of one pixel in both horizontal and vertical directions. Moreover, in few experiments, the accuracy of the system was compared with measurements taken by means of a graduated rod.

Each experiment required some preliminary operations, i.e., the definition of the control parameters to be provided to the wavemaker in order to generate the desired waves, the choice of the Vectrino Profiler software configuration, the calibration of the optical system, the leveling of the sandy bed. This last task had to be carefully performed in order to remove any ripple mark from the sandy bed and to start each experiment from an initially flat condition.

Hydrodynamic and morphodynamic measurements had to be acquired separately. Indeed, the flow measurements required a sufficiently large concentration of particles in suspension, in order to allow the acoustic signal to be reflected by the suspended particles. The morphodynamic measurements instead had to be performed in perfectly clear water to make the image formation possible on the camcorder lenses. Thus, the experimental procedure followed such a schedule:

- In the presence of clear water and starting from an initially flat bed, the waves propagated on the sandy bottom and triggered the formation of ripple bedforms. At the same time, the structured light approach was used to acquire the rippled bed images by means of a camera. The morphodynamic acquisition ended once the equilibrium was achieved, which generally occurred within 15 min.
- Once the morphodynamic measurements were performed, the water was seeded by means of talc powder and two vertical profiles were acquired, the first one located on the horizontal sandy bottom (P_1) and the other one on the sloping bed (P_2). The origin of the vertical axis was placed in correspondence to the ripple trough at the two positions P_1 or P_2. The choice of the trough was carried out in order to minimize the effects of ripple migration on the Vectrino's bottom distance. In addition, velocities were measured after the reaching of the ripples equilibrium configuration, when ripple migration reached a steady state.

3 Experiments

Fifteen experiments were performed. Twelve of these experiments used regular waves, and three used random

Table 1 Hydraulic characteristics of the performed experiments

Test name		d [m]	H, H_s [m]	T, T_m [s]	Duration [min]	Measurement type
Regular waves	Reg_1	0.145	0.067	1.23	15	hydr.+morph.
	Reg_2	0.145	0.069	1.22	15	hydr.+morph.
	Reg_3	0.145	0.071	1.01	15	hydr.+morph.
	Reg_4	0.145	0.083	1.01	30	morph.
	Reg_5	0.145	0.083	1.01	15	hydr.+morph.
	Reg_6	0.145	0.157	1.01	15	hydr.+morph.
	Reg_7	0.145	0.057	0.84	15	hydr.+morph.
	Reg_8	0.145	0.096	0.84	15	hydr.+morph.
	Reg_9	0.145	0.091	0.84	15	hydr.+morph.
	Reg_{10}	0.145	0.132	0.84	30	morph.
	Reg_{11}	0.147	0.127	0.84	15	hydr.+morph.
	Reg_{12}	0.145	0.122	0.84	15	hydr.+morph.
Random waves	Ran_1	0.136	0.085	0.90	15	morph.
	Ran_2	0.138	0.062	0.79	15	morph.
	Ran_3	0.134	0.057	0.90	15	morph.

waves characterized by TMA peak period $T_p = 1.2T_m = 0.95-1.10$ s and peak enhancement factor $\gamma = 3.3$. Velocity statistics were computed only for regular wave tests. Although, Aagaard and Hughes (2010) and Brinkkemper et al. (2017) described a procedure to phase-average random wave time series treating all the waves of the series together. In this case, a wave-by-wave analysis could be more appropriate, in order to average homogeneous components. Thus, a much longer time series should be considered and further future works can be devoted to extend these analyses to random wave experiments.

In Table 1, the experimental parameters of each test are reported; the last three rows refer to random waves. In particular, the first column indicates the test name; the second column reports the water depth along the sloping bottom at the same position where ripple characteristics were measured that sometimes slightly differed from the planned $d = 0.145$ m value; the two following columns show the wave height or the significant wave height in the case of random waves, and the mean period measured by the offshore wave gauge G_1. Finally, the last two columns report the test duration and the measurement type indicating if throughout the test hydrodynamic (hydr.) and/or morphodynamics (morph.) measurements were carried out. To verify that the 15-min test length was sufficient to reach the morphodynamic equilibrium, two tests, namely Reg_5 and Reg_{11}, were repeated by performing the measurements for 30 min (Reg_4 and Reg_{10}). The results showed no appreciable differences in terms of ripple shape between these longer tests and the corresponding 15-min tests; therefore, the other measurements were not repeated.

During every test, water elevation was measured for 2 min after the beginning of the wave propagation by all the five resistive wave gauges, as described above. The five signals were phase-averaged to obtain the ensemble wave at the five locations. In Fig. 2, an example of the water elevation η, as recorded by the wave gauge G_5 located on the sloping bed, is reported for two regular wave tests Reg_5 ($H = 0.0825$ m; $T = 1.01$ s) and Reg_9 ($H = 0.0911$ m; $T = 0.84$ s).

Figure 3a and b shows the shoaling of water waves propagated during the tests Reg_5 and Reg_9. During Reg_5 test, waves grow and partially lose their symmetry due to the interaction with the horizontal plane bed. Then, in proximity of the breaking zone, waves become considerably

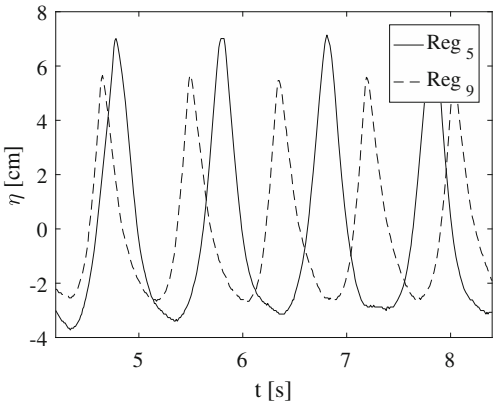

Fig. 2 Water elevation for two regular wave tests measured by wave gauge G_5 (solid line: test Reg_5: $H = 0.0825$ m; $T = 1.01$ s; dashed line: test Reg_9: $H = 0.0911$ m; $T = 0.84$ s)

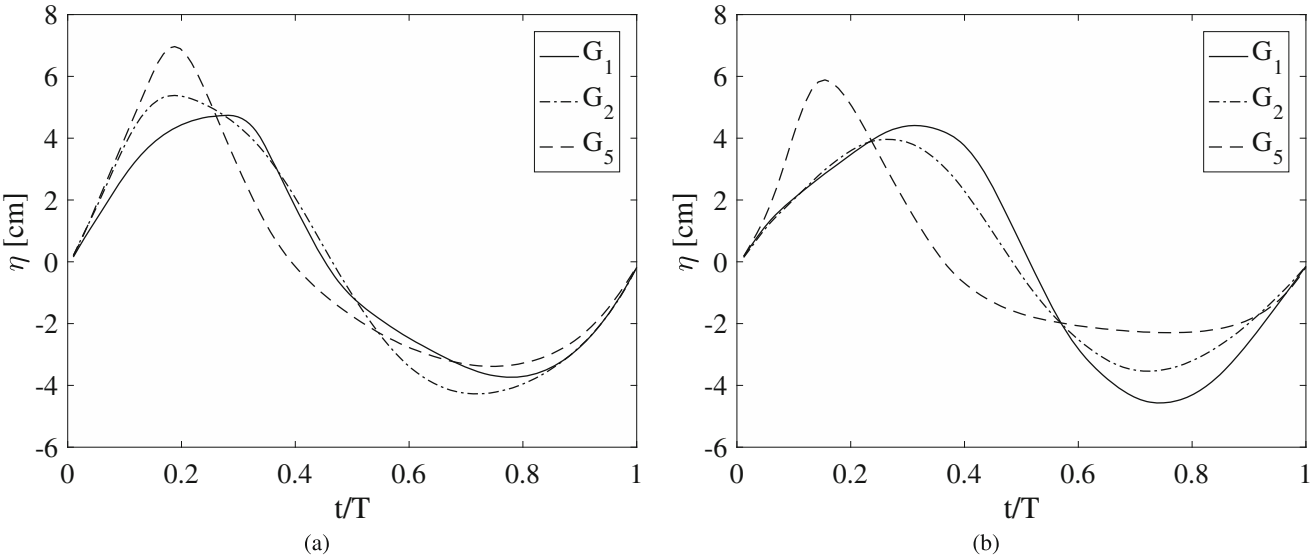

Fig. 3 Ensemble water surface elevation measured offshore (wave gauge G_1), above the plane sandy bed (wave gauge G_2) and above the sloping bed (wave gauge G_5): **a** test Reg_5 ($H = 0.0825$ m; $T = 1.01$ s); **b** test Reg_9 ($H = 0.0911$ m; $T = 0.84$ s)

skewed and asymmetric. Instead, during Reg_9, a partial wave breaking occurs above the plane bed; therefore, wave height at G_2 is smaller than at G_1. The waves become skewed and asymmetric only above the sloping beach. This is also confirmed by the water surface elevation shown in Fig. 2, where Reg_9 wave height appears to be sensibly smaller whit respect to the volume acquired by gauge G_1 and reported in Table 1.

The dimensionless parameters usually employed in the analysis of ripple dynamics are as follows:

- The relative density of sediments:

$$s = \frac{\rho_s}{\rho} \tag{1}$$

- The flow Reynolds number:

$$\text{Re} = \frac{U_0 A}{\nu} \tag{2}$$

- The sediment Reynolds number:

$$\text{Re}_d = \frac{U_0 d_{50}}{\nu} \tag{3}$$

- The mobility number:

$$\psi = \frac{U_0^2}{(s-1)\,\text{gd}_{50}} \tag{4}$$

- The Shields parameter:

$$\theta = \frac{1}{2} f_w \frac{U_0^2}{(s-1)\,\text{gd}_{50}} \tag{5}$$

- The grain roughness Shields parameter:

$$\theta_{2.5} = \frac{1}{2} f_{2.5} \psi \tag{6}$$

Where:

- ρ_s is the sediment density;
- ρ is the water density;
- U_0 is the orbital velocity amplitude;
- A is the orbital displacement amplitude;
- ν is the kinematic water viscosity;
- d_{50} is the median grain size;
- f_w is the friction factor defined as $\frac{2}{\sqrt{\text{Re}}}$ for smooth laminar flow, i.e., $\text{Re} < 3 \cdot 10^5$;
- $f_{2.5}$ is the grain roughness friction factor, as defined by Swart (1974).

In the following sections, the flow characteristics and the morphodynamic behavior of the rippled bed are analyzed.

4 Experimental results

The hydrodynamic characteristics of the flow generated by waves propagating over a sloping sandy bed together with the morphodynamic characteristics of the rippled bed that forms under the propagating waves are here analyzed.

In Table 2, the ripple characteristics at equilibrium, namely the ripple wavelength $\lambda_{\text{eq}} = \lambda_{\text{off}} + \lambda_{\text{on}}$, being λ_{off} and λ_{on} the half wavelengths in the offshore and onshore direction respectively, as shown in Fig. 1c, the ripple height η_{eq} averaged over 3–6 ripples and time averaged at the equilibrium, i.e., for the final 3 min of each test, are reported. The variable v_{15} in Table 2 is the migration velocity obtained taking the value at $t = 15$ min of the line fitting the ripple crest migration velocity v_0. The latter was

Table 2 Hydromorphodynamic characteristics of the performed experiments

Test name	λ_{eq} [cm]	η_{eq} [cm]	v_{15} [cm·min^{-1}]	U_0 [cm·s^{-1}]	A [cm]	Re [−]	Re_d [−]	ψ [−]	θ [−]	$\theta_{2.5}$ [−]
Reg_1	6.11	1.49	0.07	38.9	7.6	29711	97	37	0.22	0.37
Reg_2	5.07	1.05	0.08	31.9	6.2	19694	80	25	0.18	0.27
Reg_3	5.22	0.89	0.04	35.1	5.6	19759	88	30	0.22	0.34
$Reg_4(P_1)$	4.20	0.60	0.04	32.4	5.2	16916	81	26	0.20	0.30
$Reg_4(P_2)$	5.11	0.68	− 0.32	41.6	6.7	27832	104	43	0.26	0.45
Reg_5	5.71	0.84	0.03	45.2	7.3	32798	113	50	0.28	0.51
Reg_6	6.14	0.75	− 0.54	52.1	8.4	43671	130	67	0.32	0.64
Reg_7	3.34	0.44	− 0.17	30.9	4.1	12816	77	24	0.21	0.30
Reg_8	3.91	0.78	0.00	33.6	4.5	15079	84	28	0.23	0.34
Reg_9	4.40	0.74	− 0.20	44.2	5.9	26118	111	48	0.30	0.53
$Reg_{10}(P_1)$	3.53	0.77	0.08	32.7	4.4	14264	82	26	0.22	0.33
$Reg_{10}(P_2)$	5.03	0.73	− 0.80	42.9	5.7	24607	107	46	0.29	0.51
Reg_{11}	5.31	0.69	− 0.82	42.9	5.7	24613	107	46	0.29	0.51
Reg_{12}	4.04	0.59	− 0.43	40.0	5.3	21369	100	40	0.27	0.45
Ran_1	6.12	0.68	− 0.30	33.4	4.9	16284	84	28	0.22	0.33
Ran_2	4.28	0.62	− 0.05	24.1	3.1	7442	60	14	0.17	0.21
Ran_3	5.42	0.81	0.04	25.3	3.7	9252	63	16	0.16	0.21

obtained as the displacement observed in two successive frames, divided by the elapsed time interval. Table 2 also reports the main previously mentioned hydrodynamic parameters, and in particular, the orbital velocity amplitude U_0 just above the bottom boundary layer together with the orbital displacement amplitude A. Finally, the non-dimensional parameters, i.e., the flow Reynolds number, the sediment Reynolds number, the mobility number, the Shields parameter, and the grain roughness Shields parameter, respectively are reported. The sediment relative density is constant and equal to $s = 2.65$, and the critical Shields parameter is equal to $\theta_{crit} = 0.0415$ (Soulsby et al. 1997) throughout the experimental campaign; thus, it was not included in the table. Based on the Shields parameter, being $\theta > \theta_{crit}$, the sediment are mobilized and vortex ripples appears. Sheet flows do not occur as $\theta < 0.8$ (see Dingler and Inman 1976).

4.1 Analysis of the hydrodynamics

In to understand the effects of the sloping beach on the hydrodynamics and, in turn, on the morphodynamic processes described afterwards, an analysis of the velocity data acquired by the Vectrino Profiler at the two positions P_1 and P_2 (see Fig. 1a) was performed. Velocities were measured above the rippled bed generated by the propagation of regular or random waves after the achievement of the equilibrium configuration in terms of ripple geometry. During the tests, velocities were acquired at one vertical section, located at the ripple trough in order to reduce uncertainties in terms of bottom distance of measured velocities. Indeed, even when the equilibrium condition was reached, ripples continued oscillating around the equilibrium position throughout the test length. Hence, the distance of the transducer from the bed within a wave cycle could vary more above the ripple crest than on the trough because the last one is flatter.

In Fig. 4a the cross-shore velocities at an elevation of 1.5 cm above the bed, i.e., about 0.5 cm over ripple crest, measured during experiment Reg_5 are shown along with the moving averaged velocity U_{MA} determined by averaging over ten periods. In fact, the wave propagation gives rise to an onshore-directed mass transport between wave crest and trough that in a two-dimensional situation must be compensated by a negative (offshore-directed) steady current that can be here observed throughout the duration of the tests. Here, for the sake of clarity, only a short part of Reg_5 test is represented in the figure. Similar results were achieved throughout the other tests. The steady current U_{AVG}, averaged over the whole test duration, measured in all the performed regular wave experiments above the sloping bed, just outside the bottom boundary layer is summarized in Fig. 4b. All the analyzed wave conditions produce offshore-directed-averaged velocities. In particular, the highest negative velocities occurred for Reg_{10} and Reg_{11} tests. These tests are characterized by the

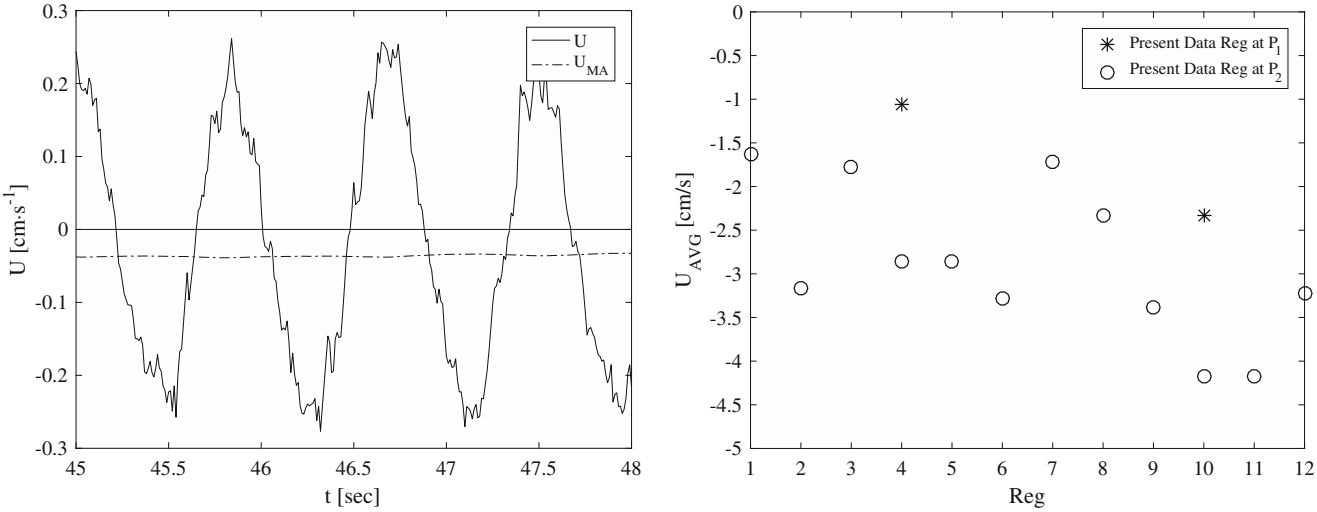

Fig. 4 **a** Cross-shore velocities measured at position P_1, test Reg_5 ($H = 0.0825$ m; $T = 1.01$ s)U indicates the instantaneous velocity measured by the Vectrino profiler at one elevation, U_{MA} indicates the moving averaged velocity over a ten-period time span; **b** outer flow-averaged velocities measured at position P_1 and P_2 throughout regular wave tests

highest values of the parameter H^2/T, which is related to the mass transport (Dean and Dalrymple 1991), together with the highest negative migration velocities (see Table 2).

The signal acquired by each cell of the Vectrino Profiler was analyzed by a zero up-crossing method to obtain the phase-averaged velocity profiles.

For sake of brevity, few tests were selected in order to provide an overview of the observed features. In particular, Figs. 5, 6, and 7 depict the velocity profiles of the experiments Reg_3, Reg_5, and Reg_{11}, respectively at the positions P_1 (plane bed) and P_2 (sloping bed). The velocity profiles are shown at four phases: $\pi/2$, π, $3\pi/2$, 2π on the plane bed, and at two more phases, namely the ones at which the maximum and the minimum velocities are observed, at P_2 position. Indeed, on the sloping bed, due to wave asymmetry the positive peak occurs at $\phi = 0.44\pi, 0.44\pi, 0.37\pi$ and the negative peak at $\phi = 1.31\pi, 1.37\pi, 1.44\pi$ during Reg_3, Reg_5, and Reg_{11} test, respectively. Thus, an anticipation of both velocity maxima and minima occurs on the sloping bed with respect to the horizontal bed case. Moreover, the velocity profile averaged over the entire wave period is also shown. Because

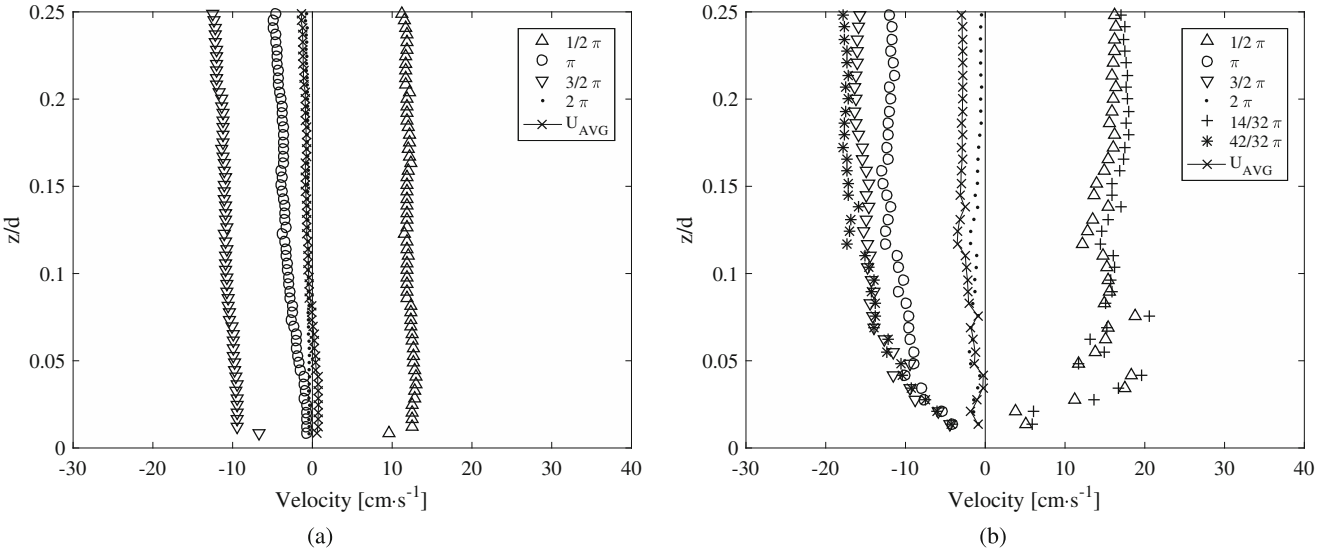

Fig. 5 Phase-averaged velocity profiles during test Reg_3 ($H = 0.0713$ m; $T = 1.01$ s): **a** position P_1; **b** position P_2. Onshore-directed velocities are assumed positive

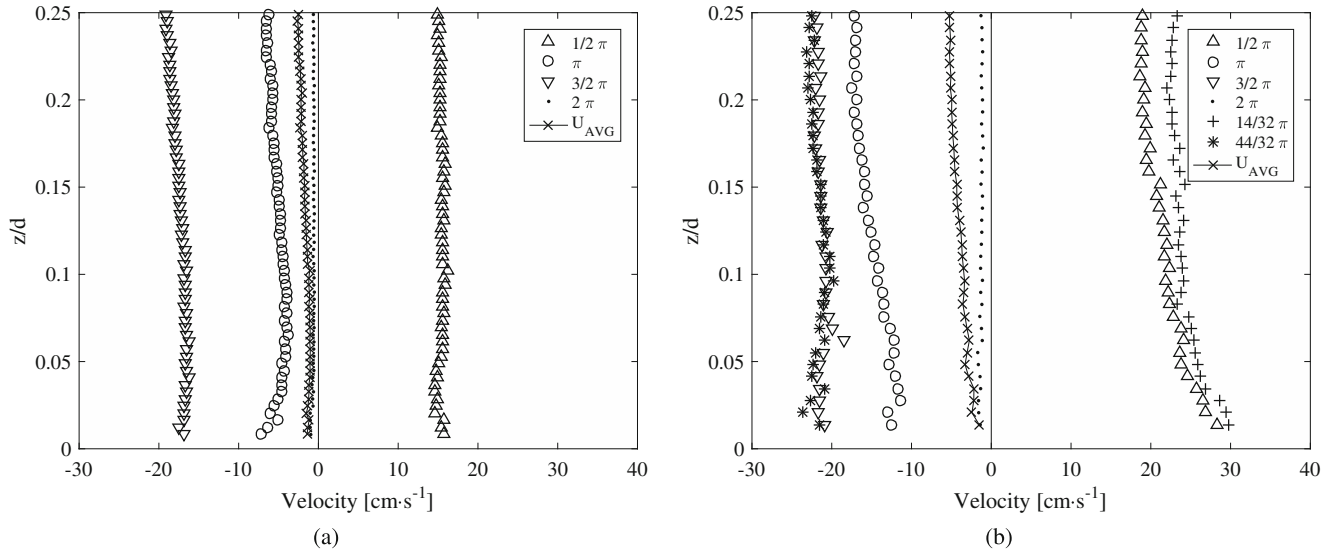

Fig. 6 Phase-averaged velocity profiles during test Reg_5 ($H = 0.0825$ m; $T = 1.01$ s): **a** position P_1; **b** position P_2. Onshore-directed velocities are assumed positive

of the wave asymmetry, zero down-crossing is reached before the π phase; therefore, at π, the velocities are already negative.

Velocity profiles are rather symmetrical on the horizontal plane bed and strongly asymmetrical over the sloping bed. Indeed, at P_1, velocities at $\pi/2$ are slightly smaller than velocities at $3\pi/2$. Averaged velocities are slightly negative throughout the profile, except close to the bottom for Reg_3 test, where average velocity turns to zero, possibly leading toward an onshore-directed steady streaming (see Longuet-Higgins 1953). Here, this phenomenon is not visible due to the discarding of the data within 2 mm from the bed. At P_2, the average velocity is considerably negative to compensate the onshore wave drift, whereas the maximum velocities are larger than the minimum ones throughout the water column. The velocity asymmetry is coherent with the asymmetry of the ensemble-averaged waves shown in Fig. 3, which exhibit higher and more peaked crests with smaller and broader troughs. Following the results of Scandura et al. (2016), a greater acceleration skewness parameter $\beta = \frac{\dot{u}_{max}}{\dot{u}_{\max} - \dot{u}_{\min}}$, $\dot{u}_{\max}$ and $\dot{u}_{\min}$ being the maximum and minimum accelerations during the cycle respectively, explains the higher offshore-directed average velocities achieved during Reg_{11} test ($\beta = 0.62$) when compared with Reg_5 ($\beta =$

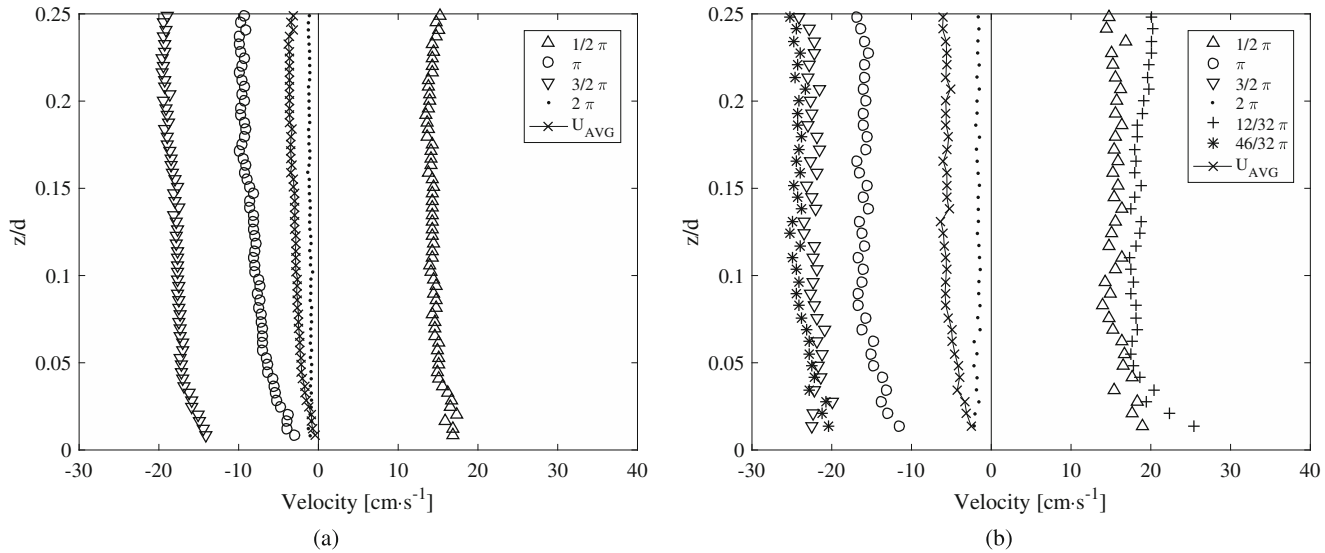

Fig. 7 Phase-averaged velocity profiles during test Reg_{11} ($H = 0.1270$ m; $T = 0.84$ s): **a** position P_1; **b** position P_2. Onshore-directed velocities are assumed positive

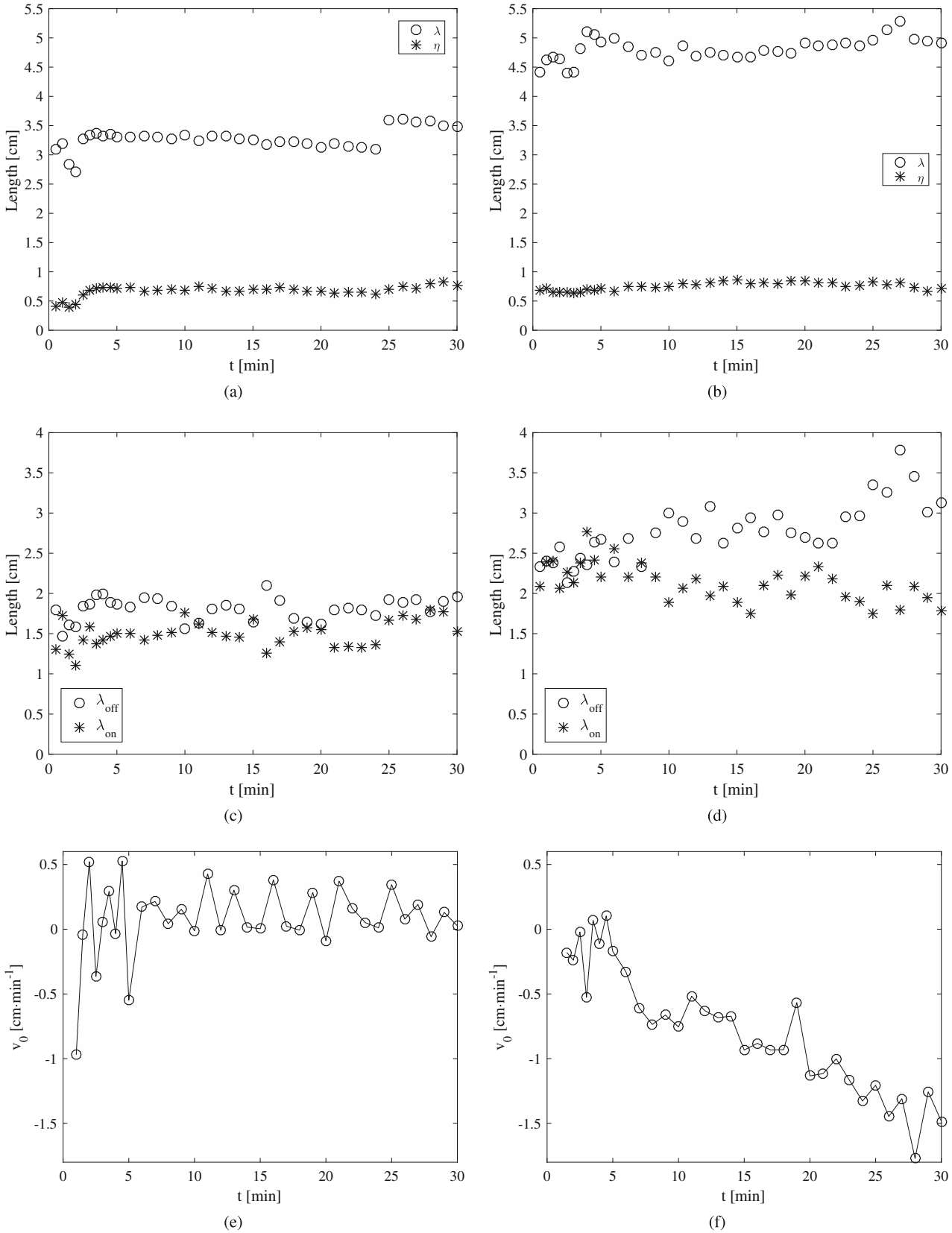

Fig. 8 Morphodynamic evolution during 30-min long test Reg_{10} ($H = 0.1270$ m; $T = 0.84$) at P_1 (left panel) and P_2 (right panel): **a**, **b** wavelength λ and height η time evolution; **c**, **d** half wavelengths λ_{on} and λ_{off} time evolution (see sketch in Fig. 1c); **e**, **f** ripple crests migration velocity v_0 time evolution

0.61) and Reg_3 ($\beta = 0.58$). Such evidence occurred, as it can be observed in Figs. 5, 6, and 7, where a negative period-averaged velocity is present at all the elevations. This phenomenon is due to a mechanism similar to that described in Scandura (2007) and Cavallaro et al. (2011) and Scandura et al. (2016). Due to the large wave asymmetry (see Fig. 3), the intensity of turbulence is different in the two half-cycles. Therefore, the time average of the Reynolds stresses do not vanish. The mean Reynolds stresses are balanced by the mean viscous stresses due to an offshore steady current. Finally, velocity profiles acquired at position P_2 show larger velocities than those measured at position P_1, where the water is deeper. This also depends on the shoaling process that concentrates the energy flux on a smaller water depth (see Petrotta et al. 2017a, b). Velocity increase causes the growth of the turbulence intensity that, in turn, produces the thickening of the boundary layer, which is clearly visible in Fig. 5b.

4.2 Morphodynamic analysis

Bedform characteristics were also investigated starting from their first appearance to the reaching of an equilibrium condition. In this section, both the evolution and the equilibrium conditions are discussed.

4.2.1 Bedform evolution

The ripple morphodynamics was measured both on the plane bed (position P_1) and on the sloping bed (position P_2) throughout the 30-min long tests Reg_4 and Reg_{10}; in all the other tests, the morphodynamics was acquired only at position P_2.

As an example, results of Reg_{10} test are summarized in Fig. 8. Ripple marks appeared after the propagation of few tens of waves and almost simultaneously on the horizontal and on the sloping bed. Within 5 min, ripple length and height reached the equilibrium condition, both along the plane and the sloping bed (Fig. 8a, b respectively). The discontinuity in ripple length diagram together with the growth of mean height (25 min, position P_1) were produced by the merging of two adjacent ripples. Because of higher near-bed velocities measured above the sloping bed, ripples were longer and flatter at position P_2 ($\lambda_{eq} \approx 5$ cm, $\eta_{eq} \approx 0.7$ cm) than at position P_1 ($\lambda_{eq} \approx 3.5$ cm, $\eta_{eq} \approx 0.8$ cm). At location P_1, regular waves generated symmetric ripples whose half wavelengths did not change considerably throughout the test (see Fig. 8c). Instead, because of wave asymmetry, after approximately 8 min from the start of the experiment, ripples above the sloping bed (Fig. 8d) became asymmetric. Indeed, the offshore half wavelength λ_{off} started growing, while the onshore half wavelength λ_{on} decreased (see Fig. 1c). Such a phenomenon led ripple onshore flanks to become steeper than offshore flanks. Notwithstanding, the ripple wavelength reaches a constant value after the first minutes, the semi-half lengths tend to diverge, with λ_{on} becoming shorter and λ_{off} larger. Since the shape of the ripple profile continues to change even after the reaching of equilibrium conditions, this phenomenon has repercussion on the migration velocity.

Figure 8e, f shows the migration velocities measured at the two test positions. As before mentioned, migration velocity was obtained as the ratio between the ripple crest displacement, recorded during each time interval, and the elapsed time interval, i.e., 1 min. During the first 5 min of tests, this time lapse was halved in order to better describe

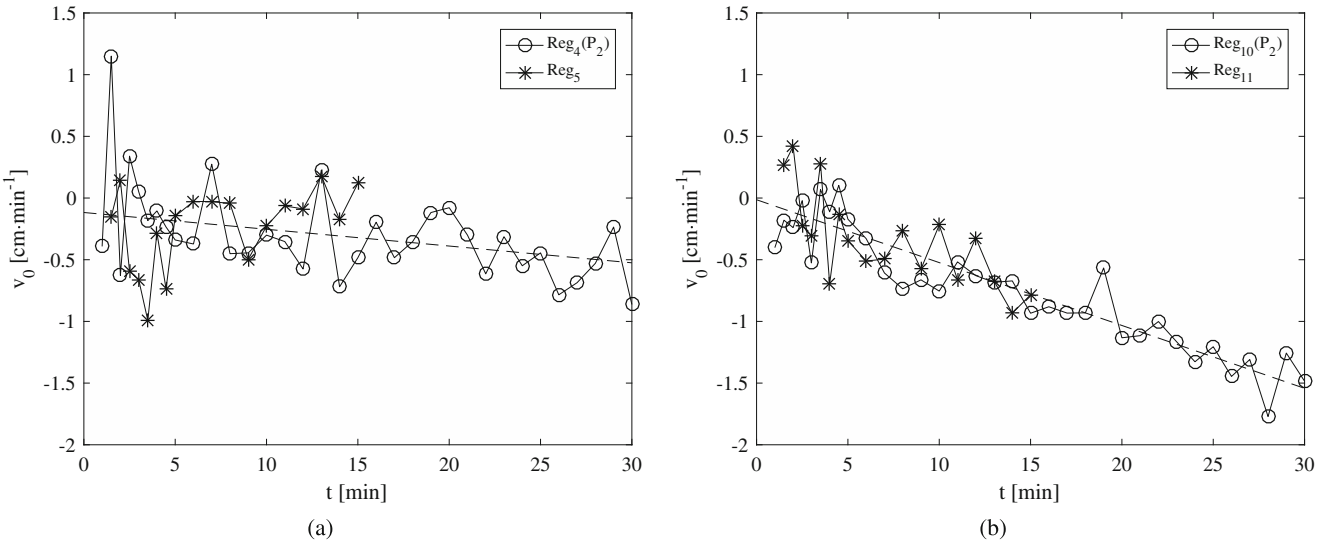

Fig. 9 Comparison between the migration velocity of ripples v_0 at position P_2: **a** Reg_4 and Reg_5 tests ($H = 0.0825$ m; $T = 1.01$ s); **b** Reg_{10} and Reg_{11} tests ($H = 0.1270$ m; $T = 0.84$ s)

the ripple growth from the flat bed. At the very beginning of some tests, e.g., Reg_{10} (position P_1), ripple crests migrated alternately onshore and offshore (see Fig. 8e), reaching the equilibrium condition after about 10 min from the beginning of the test. Instead, along the sloping bed, these velocities were offshore directed throughout the test and did not converge to a fixed value (see Fig. 8f).

In most of the morphodynamic tests on the sloping bed, as a consequence of the dominant offshore steady current discussed in the previous section, the migration velocity shows negative values that decrease in time with a regular trend (Fig. 8). More specifically, superimposing the migration velocities obtained with the same hydrodynamic conditions respectively for Reg_5 and Reg_{11}, lasting 15 min, to those of $\mathrm{Reg}_4(P_2)$ and $\mathrm{Reg}_{10}(P_2)$, lasting 30 min, it is possible to observe that (i) each of the two couples of curves are superimposable, thus assessing the repeatability of the experiment; (ii) there is not asymptotycal tendency leading to a constant value, at least within the investigated time span (see in Fig. 9a and b). As mentioned before, throughout the tests duration, ripples reached the equilibrium value both in terms of wavelength and height but not in terms of ripple asymmetry ($\lambda_{\mathrm{off}}/\lambda_{\mathrm{on}}$); the migration velocity (v_0) is naturally affected by the change of the shape of the ripple profile, preventing the reach of an asymptotical value.

In order to make the data homogeneous, a trend curve interpolating the v_0 data was superimposed, where the already mentioned quantity v_{15} indicates the estimated value at 15 min. In the following section, these quantities

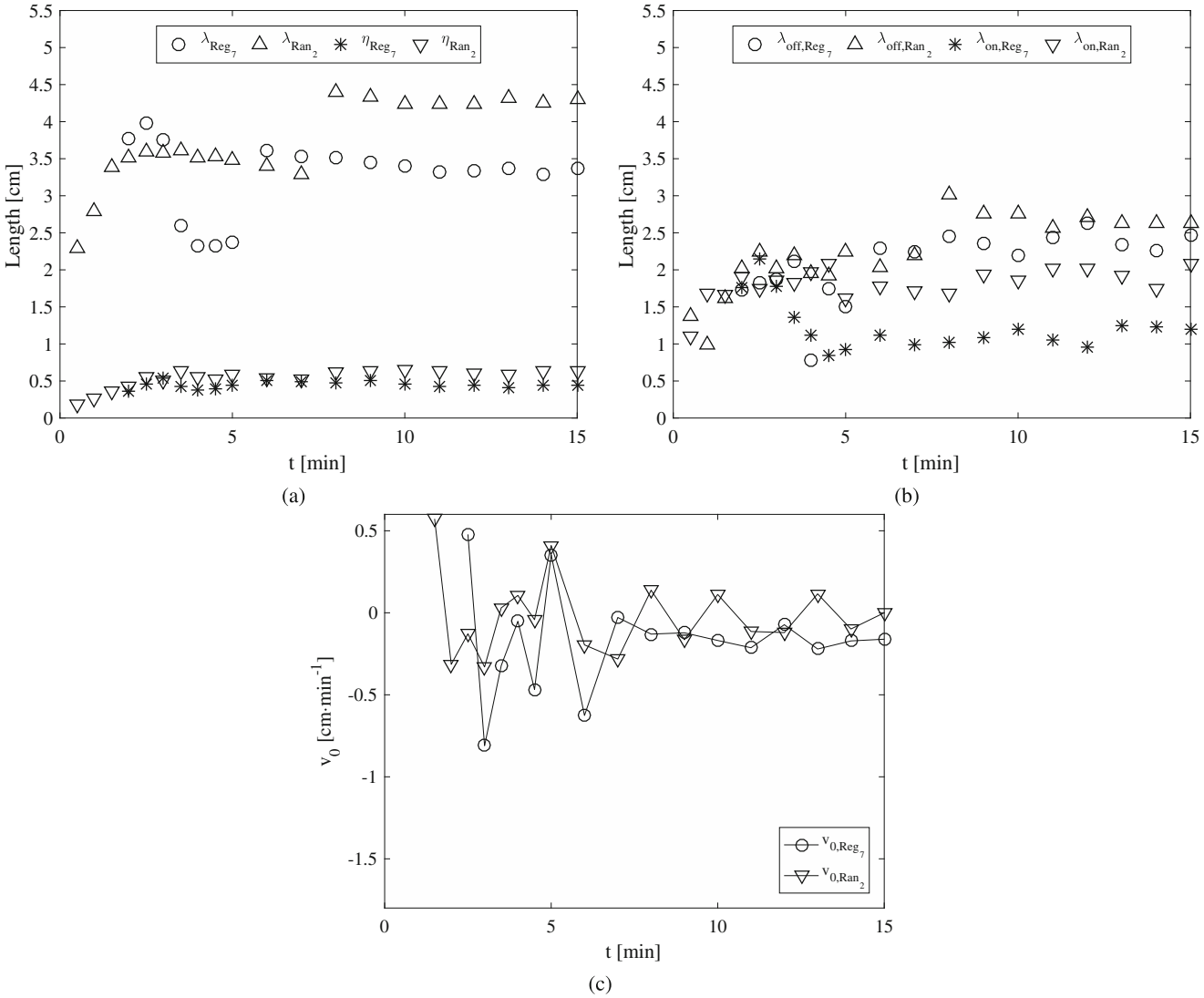

Fig. 10 Comparison between Reg_7 test ($H = 0.0573$ m, $T = 0.8412$ s) and Ran_2 test ($H_s = 0.063$ m, $T_m = 0.8041$ s) at P_2: **a** ripple wavelength λ and height η time evolution; **b** ripple half wavelengths $\lambda_{\mathrm{on}}$and λ_{off} time evolution, see picture in Fig. 1c; **c** ripple crests migration velocity v_0 time evolution

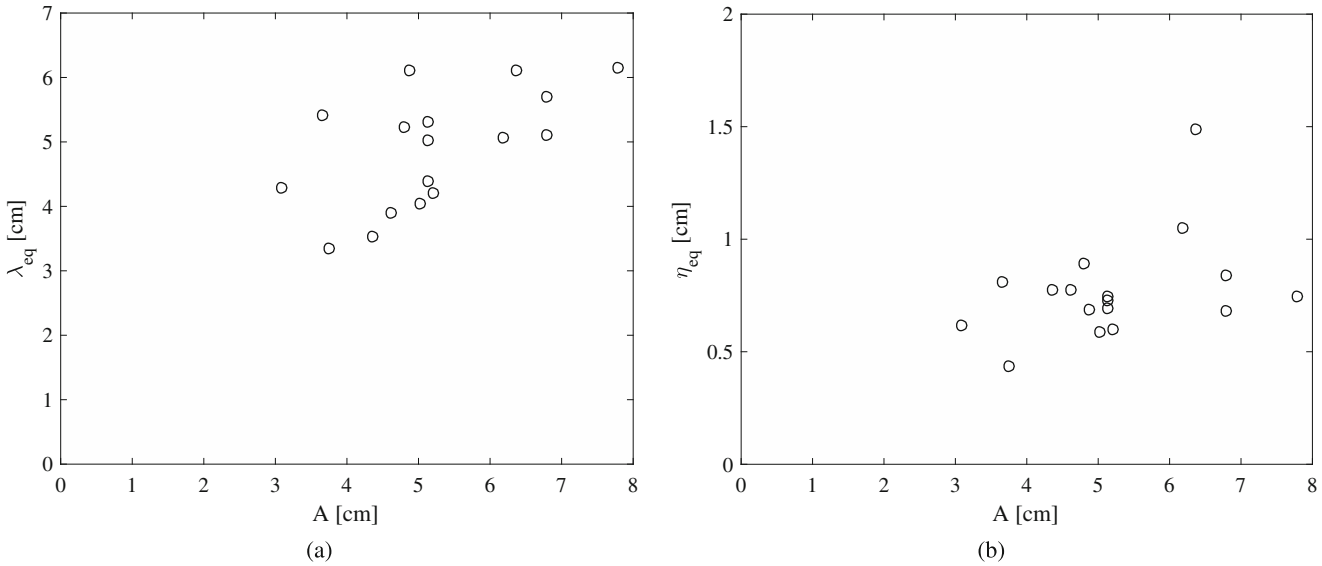

Fig. 11 Ripple wavelength λ_{eq} **a** and height η_{eq} **b** behavior versus orbital displacement amplitude A

observed after 15 min of experiment are referred to as equilibrium conditions and are discussed as a function of the main hydrodynamic characteristics.

It is worth recalling that Doucette and O'Donoghue (2006) analyzed the evolution of a flat bed covered by coarse sand ($d_{50} = 0.44$ mm) and proposed the following equation to estimate the number of flow cycles needed to reach the equilibrium n_e:

$$n_e = \exp(0.036\psi + 7.44). \tag{7}$$

According to the previous relation, the mobility numbers measured throughout this experimental campaign would lead to the equilibrium in time intervals of about 1–2 h; however, during the present tests, ripple wavelength and height reached the equilibrium condition in about 10 min. Indeed, after such time interval, no appreciable variation of these measured quantities was observed. On the contrary, the migrating velocities showed a linear trend at least during the investigated time span.

The negative ripple migration is caused by a net suspended load flux that, in turn, follows the offshore-directed flow (undertow)(see Fuhrman et al. 2009b), which balances the onshore flux of water generated between the trough and the crest of the asymmetric and/or skewed waves. The migration is more pronounced above the sloping bed than above the horizontal bed due to greater negative

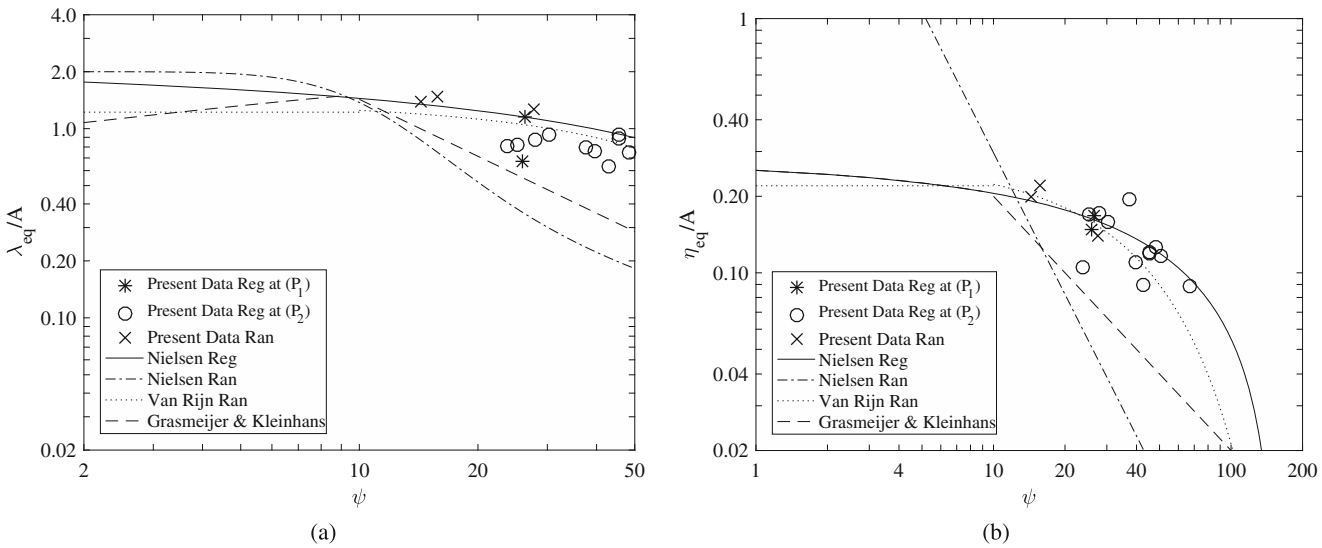

Fig. 12 Comparison of non-dimensional ripple geometry data with ripple predictor models: **a** ripple wavelength λ; **b** ripple height η_{eq}

period averaged velocities. Moreover, the measured skewed and asymmetric waves lead to asymmetric bedforms.

Finally, the morphodynamic response of the sloping bed induced by the random waves propagated during Ran_2 test ($H_s = 0.063$ m, $T_m = 0.8041$ s) was compared to the one induced by the regular waves propagated during Reg_7 test ($H = 0.0573$ m, $T = 0.8412$ s) (see Fig. 10). These results are in agreement with O'Donoghue et al. (2006) who observed that, at low mobility number, dimensions of ripples triggered by regular and random waves with comparable flow orbital amplitude are similar. Neglecting local effects, such as the ripple merging (at 6 and 8 min after the beginning of respectively Reg_7 and Ran_2) and split (at 3 min 30 s after the beginning of Reg_7) ripple wavelength and height were comparable throughout the tests (see Fig. 10a), even though the regular wave wavelength is slightly smaller than the random wave one. At the very beginning of both tests, ripples were symmetric; indeed, ripple half wavelengths shown in Fig. 10b were about 2 cm long for both tests. After 4 min, ripple onshore half wavelength started decreasing in Reg_7 whereas it does not change significantly in Ran_2; the offshore half wavelength slightly increase both in Ran_2 and Reg_7 tests. Such an asymmetry agrees with migration velocities plotted in Fig. 10c. Ripples migrated mainly offshore from 1 min up to 6 min and became almost stable after 7 min from the beginning of both tests.

4.2.2 Equilibrium conditions

In Fig. 11, the ripple characteristics at the equilibrium obtained in the present campaign are plotted as a function of the orbital displacement amplitude A. In particular, ripple wavelength increases for higher values of A, as the bed is subject to a larger excursion, and thus the fluid particles tend to stretch the ripple wavelengths. On the other hand, ripple height does not seem to sensibly change with A.

The measured equilibrium characteristics of ripples, for the case of both regular and random waves, were compared with the results provided by some literature ripple predictors. Ripple geometry was measured both above the sloping bed (position P_2) and, in the case of few regular wave tests, also above the horizontal bed (position P_1).

More in detail, ripple wavelength, height and steepness at equilibrium were compared with the predictor models of Nielsen (1981), Van Rijn (1993), and Grasmeijer and Kleinhans (2004) in Figs. 12 and 13.

The non-dimensional regular wave ripple length, reported in Fig. 12a, is adequately estimated by the regular wave (Nielsen 1981) predictor, even though with a slight overprediction providing the lowest root-mean-squared error (RMSE = 0.25) among the considered ripple predictors. Moreover, the regular wave (Nielsen 1981) model fit accurately the ripple height data showed in Fig. 12b with a RMSE = 0.03.

In agreement with O'Donoghue et al. (2006) and Faraci and Foti (2002), in random wave cases the Nielsen (1981) model is in poor agreement with measured wavelength. Instead, the Van Rijn (1993) model predicts accurately both the non-dimensional ripple length (RMSE = 0.24) and height (RMSE = 0.02).

The non-dimensional ripple wavelength overestimation of the Nielsen (1981) model has an effect in ripple steepness prediction under regular waves showed in Fig. 13a as a

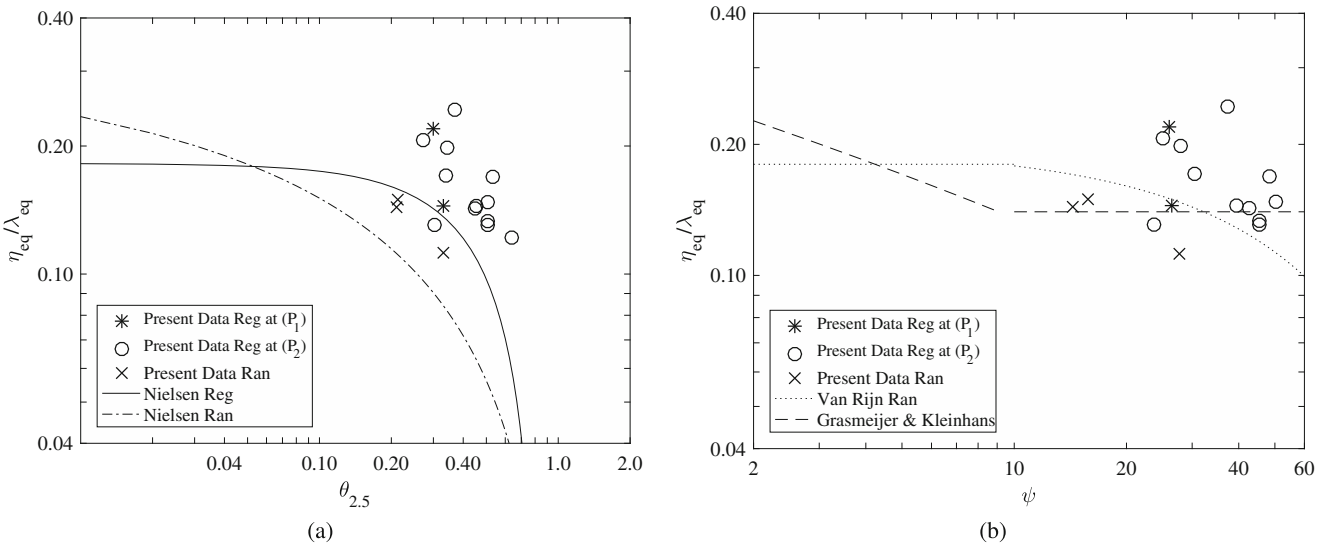

Fig. 13 Ripple steepness predictor models: **a** comparison with Nielsen (1981); **b** comparison with Grasmeijer and Kleinhans (2004) and Van Rijn (1993)

function of the grain roughness Shield's parameter. Indeed, it is observed in general that the dimensionless steepness is underpredicted. Also, the equation proposed by Grasmeijer and Kleinhans (2004) and based on the Nielsen (1981) predictor underestimates the ripple steepness in terms of the mobility number (see Fig. 13b).

As shown in Section 4.1, the sloping beach induces negative-averaged velocities throughout the water depth. Such an offshore-directed current makes the ripples asymmetric with the offshore half wavelength larger than the onshore one. Following (Blondeaux et al. 2015), such a phenomenon can be observed relating the asymmetry index $\lambda_{off}/\lambda_{on}$ to the ratio between the averaged current velocity U_{AVG} and the near-bed orbital velocity U_0, both measured directly above the bottom boundary layer. In Fig. 14a, data measured throughout the regular wave tests are compared with data collected by Blondeaux et al. (2015) showing the crucial role exerted by the sloping bed in ripple asymmetry. Indeed, although the mass transport velocity did not vary considerably throughout the experiments, ripples measured above the sloping bed are noticeably asymmetric ($1.25 < \frac{\lambda_{off}}{\lambda_{on}} < 2.8$), whereas ones measured above the horizontal plane bed are symmetric ($\frac{\lambda_{off}}{\lambda_{on}} \sim 1$). It is however possible to observe that $\lambda_{off}/\lambda_{on}$ shows a tendency to increase as far as the exceedance of U_{max} on U_{min} increases as well. Indeed, even though the steady drift is offshore-directed and drives the ripples to migrate offshore; however, as shown in the

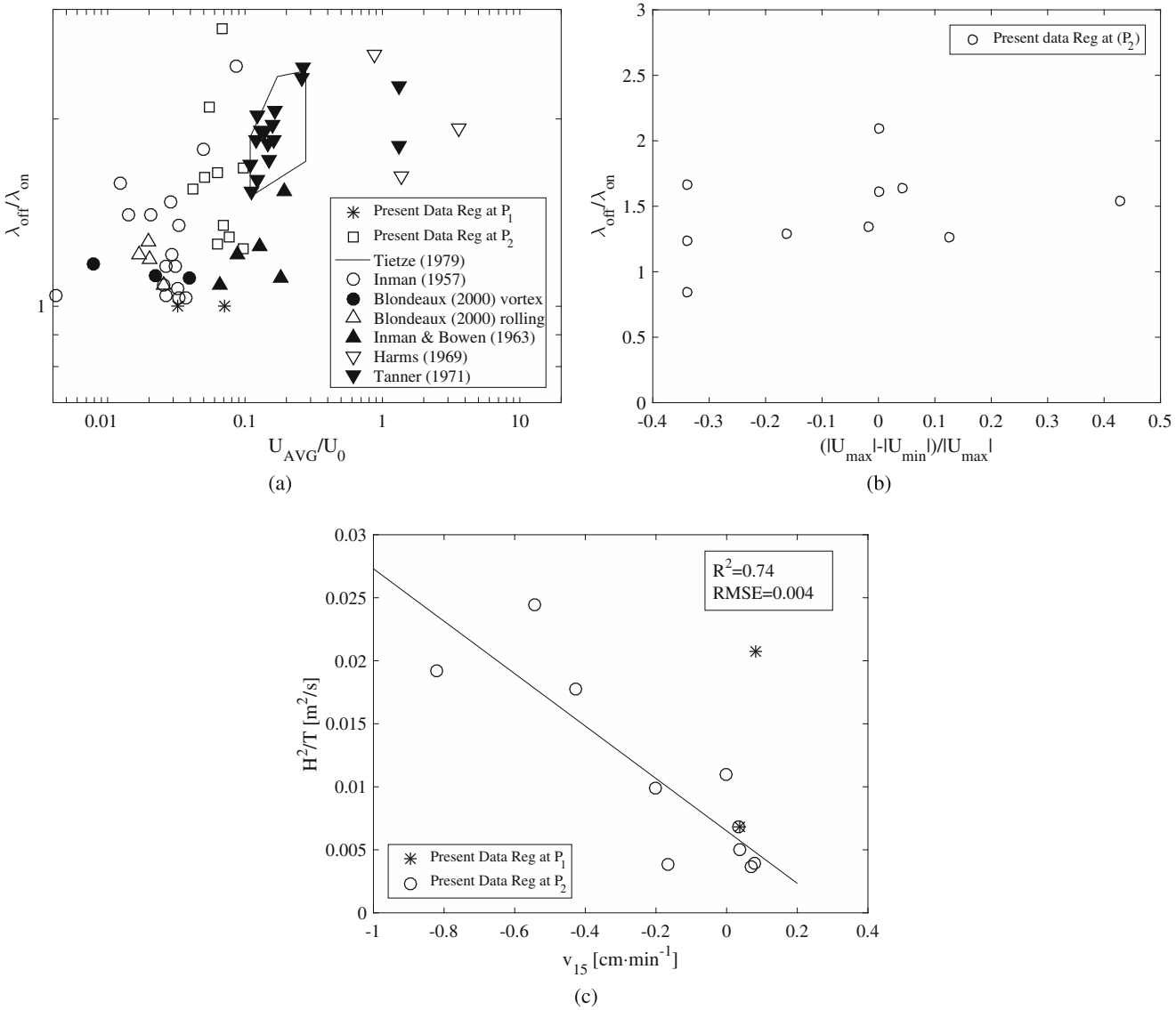

Fig. 14 Relationship between ripple morphodynamics and flow hydrodynamics: **a** ripple symmetry index plotted versus the ratio between outer flow-averaged velocity and maximum near-bed orbital velocity; **b** ripple symmetry index plotted versus the ratio between outer flow maximum minus minimum velocity and maximum outer flow velocity; **c** ripple migration velocity v_{15} and H^2/T

previous section, the maximum onshore velocity is higher than the minimum one, and it leads the offshore flank to increase at the expenses of the onshore one.

Finally, the migration velocity expressed in terms of the variable v_{15} is affected by the undertow. Indeed, a strong offshore-directed mean velocity produces a noticeable negative migration velocity (see Fig. 14c). In Fig. 14c, the line fitting migration velocities at position P_2 is also reported, showing a reasonable agreement with the measured data. The undertow current, which is proportional to H^2/T (Dean and Dalrymple 1991) can induce significant migration velocities.

5 Conclusions

An experimental campaign was performed in order to investigate the hydrodynamics induced by sea waves propagating over a sloping beach and its effects on a cohesionless bottom. In order to investigate how the interaction between the waves and the sloping bed affects the hydrodynamics, the flow field was measured by means of a Vectrino Profiler. The morphodynamic evolution of the bed was detected by means of a structured light technique, which allowed to determine the time development of the ripple height, wavelength and migration rate.

Approaching to the sloping bottom, waves become strongly asymmetrical, with flat, wide troughs and sharp crests as measured by the resistive wave gauges deployed into the flume. Phase-averaged velocity profiles above the horizontal plane bed are pretty symmetrical, whereas profiles measured above the sloping bed are substantially asymmetric due to the asymmetry of the surface wave. Indeed, moving from offshore to onshore, at the first measuring position the maximum and minimum velocity are comparable throughout the water depth and period-averaged velocities are slightly offshore-directed; at the second measuring position, velocities at $\pi/2$ are larger than at $3\pi/2$ to compensate the high offshore-directed velocities throughout the water column. Moreover, the maximum velocity is reached at phases between 0.37π and 0.44π, while the minimum at phases between 1.31π and 1.44π during Reg_3, Reg_5 and Reg_{11} test, respectively, hence anticipating the phases at which maxima and minima occur on the horizontal bed.

It was found that ripples start to appear on the sandy bed after few wave cycles from the beginning of the experiment. The sloping bed strongly affects both the ripple shape and the migration velocity. Indeed, ripples measured at the sloping bed are strongly asymmetric with offshore half wavelengths often larger than onshore ones; in addition, ripples are longer and flatter than the ones measured above the horizontal plane bed. The ripple asymmetry is driven by the higher value of $U_{\max}$ with respect to $U_{\min}$ that makes bedforms to lean towards the beach. Moreover, after a brief transient where ripples migrate alternatively in both directions, ripples measured on the horizontal plane bed quickly converge at an equilibrium value, where the migration velocity is negligible. Instead, the migration velocity of ripples measured above the sloping bed is usually offshore-directed throughout the duration of the tests and does not reach an equilibrium value in the investigated time span. This occurs because, as soon as ripples start to migrate, the steady component originated by recirculation cells is added to the offshore-directed mass transport velocity, giving rise to an increase in the migration velocity itself. The ripple shape and migration velocities generated by a random waves propagating on the sloping beach were similar to the ones triggered by regular waves energetically equivalent to the significant random waves.

The effects of the sloping beach on the ripple half wavelengths and asymmetry are in a fairly good agreement with several ripple predictors. In particular, at the equilibrium, the ripple predictors developed for horizontal beds well describe the sloping bed morphodynamics. In particular, they correctly predict the ripple height; they slightly overestimate the ripple wavelength triggered by regular waves and accurately describe the random wave wavelength.

Acknowledgements The authors wish to thank the anonymous Referees and the Associate Editor for their valuable comments.

Funding information This research has been partially funded by the Italian Ministero dell'Istruzione, dell'Università e della Ricerca through the PRIN 2012 Project 'Hydromorphodynamic modeling of coastal processes for engineering purposes'.

References

Aagaard T, Hughes MG (2010) Breaker turbulence and sediment suspension in the surf zone. Mar Geol 271(3-4):250–259

Bagnold RA (1946) Motion of waves in shallow water. Interaction between waves and sand bottoms. In: Proceedings of the Royal Society of London A: Mathematical, Physical and Engineering Sciences, The Royal Society, vol 187, pp 1-18

Bijker EW, Kalkwijk JPT, Pieter T (1974) Mass transport in gravity waves on a sloping bottom. In: Coastal engineering proceedings, ASCE, 1 pp 447-465

Blondeaux P (1990) Sand ripples under sea waves. Part i: ripple formation. J Fluid Mech 218(1):1–17

Blondeaux P, Foti E, Vittori G (2000) Migrating sea ripples. European Journal of Mechanics-B/Fluids 19(2):285–301

Blondeaux P, Foti E, Vittori G (2015) A theoretical model of asymmetric wave ripples. Philos Trans R Soc Lond A Math Phys Eng Sci 373(2033):20140,112

Brinkkemper J, Bakker A, Ruessink B (2017) Intrawave sand suspension in the shoaling and surf zone of a field-scale laboratory beach. J Geophys Res Earth Surf 122(1):356–370

Cavallaro L, Scandura P, Foti E (2011) Turbulence-induced steady streaming in an oscillating boundary layer: on the reliability of turbulence closure models. Coast Eng 58(4):290–304

Dean RG, Dalrymple RA (1991) Water wave mechanics for engineers and scientists, vol 2. World Scientific Publishing Company

Dingler JR, Inman DL (1976) Wave-formed ripples in nearshore sands. Coastal Engineering Proceedings 1(15):2109–2126

Doucette J, O'Donoghue T (2006) Response of sand ripples to change in oscillatory flow. Sedimentology 53(3):581–596

Faraci C (2018) Experimental investigation of the hydro-morphodynamic performances of a geocontainer submerged reef. J Waterw Port Coast Ocean Eng 144(2):1–14

Faraci C, Foti E (2002) Geometry, migration and evolution of small-scale bedforms generated by regular and irregular waves. Coast Eng 47(1):35–52

Faraci C, Foti E, Marini A, Scandura P (2012) Waves plus currents crossing at a right angle: sandpit case. J Waterw Port Coast Ocean Eng 138(5):339–361

Fuhrman DR, Fredsøe J, Sumer BM (2009a) Bed slope effects on turbulent wave boundary layers: 1. Model validation and quantification of rough-turbulent results. J Geophys Res Oceans 114(C3):1–16

Fuhrman DR, Fredsøe J, Sumer BM (2009b) Bed slope effects on turbulent wave boundary layers: 2. Comparison with skewness, asymmetry, and other effects. J Geophys Res Oceans 114(C3): 1–19

Goring DG, Nikora VI (2002) Despiking acoustic doppler velocimeter data. J Hydraul Eng 128(1):117–126

Grasmeijer B, Kleinhans M (2004) Observed and predicted bed forms and their effect on suspended sand concentrations. Coast Eng 51(5):351–371

Hsu TJ, Hanes DM (2004) Effects of wave shape on sheet flow sediment transport. J Geophys Res Oceans 109(C5):1–15

Koca K, Noss C, Anlanger C, Brand A, Lorke A (2017) Performance of the Vectrino Profiler at the sediment–water interface. J Hydraul Res 55(4):1–9

Liu Y, Faraci C (2014) Analysis of orthogonal wave reflection by a caisson with open front chamber filled with sloping rubble mound. Coast Eng 91:151–163

Longuet-Higgins MS (1953) Mass transport in water waves. Philos Trans R Soc A Math Phys Eng Sci 245(903):535–581

Mansard EP, Funke E (1980) The measurement of incident and reflected spectra using a least squares method. Coast Eng 1980:154–172

Nielsen P (1981) Dynamics and geometry of wave-generated ripples. J Geophys Res Oceans 86(C7):6467–6472

O'Donoghue T, Doucette J, Van der Werf J, Ribberink J (2006) The dimensions of sand ripples in full-scale oscillatory flows. Coast Eng 53(12):997–1012

Petrotta C, Faraci C, Scandura P, Foti E (2017a) The flow over asymmetrical ripples: an experimental investigation on the hydrodynamics behavior. In: Proceedings of Coastal Dynamics

Petrotta C, Faraci C, Scandura P, Foti E (2017b) Hydrodynamics above fixed asymmetrical ripples. Proc SCACR pp 6

Scandura P (2007) Steady streaming in a turbulent oscillating boundary layer. J Fluid Mech 571:265–280

Scandura P, Faraci C, Foti E (2016) A numerical investigation of acceleration-skewed oscillatory flows. J Fluid Mech 808:576–613

Sleath JF (1984) Sea bed mechanics. Wiley, New York

Soulsby R, Whitehouse R et al (1997) Threshold of sediment motion in coastal environments. In: Pacific Coasts and Ports' 97: Proceedings of the 13th Australasian Coastal and Ocean Engineering Conference and the 6th Australasian Port and Harbour Conference; vol 1, Centre for Advanced Engineering, University of Canterbury pp 145

Sumer BM, Laursen TS, Fredsøe J (1993) Wave boundary layer in a convergent tunnel. Coast Eng 20:317–342

Swart DH (1974) Offshore sediment transport and equilibrium beach profiles PhD thesis. Delft University of Technology, Delft

Thomas R, Schindfessel L, McLelland S, Creëlle S, De Mulder T (2017) Bias in mean velocities and noise in variances and covariances measured using a multistatic acoustic profiler: the nortek vectrino profiler. Meas Sci Technol 28(7):075,302

Van Rijn LC (1993) Principles of sediment transport in rivers, estuaries and coastal seas, vol 1006. Aqua publications Amsterdam

Van der Werf J, Doucette J, O'Donoghue T, Ribberink J (2007) Detailed measurements of velocities and suspended sand concentrations over full-scale ripples in regular oscillatory flow. J Geophys Res Earth Surf 112(F2):1–18

van der Zanden J, O'Donoghue T, Hurther D, Cáceres I, McLelland SJ, Ribberink JS et al (2017) Large-scale laboratory study of breaking wave hydrodynamics over a fixed bar. J Geophys Res Oceans 122(4):3287–3310

Wengrove M, Foster D (2014) Field evidence of the viscous sublayer in a tidally forced developing boundary layer. Geophys Res Lett 41(14):5084–5090

Yoon HD, Cox DT (2010) Large-scale laboratory observations of wave breaking turbulence over an evolving beach. J Geophys Res Oceans 115(C10):1–16